HOKKAIDO UNIVERSITY

Title	Identification of Air Masses Responsible for Warm Events on the East Antarctic Coast
Author(s)	Kurita, Naoyuki; Hirasawa, Naohiko; Koga, Seizi et al.
Citation	SOLA (Scientific Online Letters on the Atmosphere), 12, 307-313 https://doi.org/10.2151/sola.2016-060
Issue Date	2016-12-07
Doc URL	https://hdl.handle.net/2115/64668
Type	journal article
File Information	12_2016-060(5).pdf

Hokkaido University Collection of Scholarly and Academic Papers : HUSCAP

Identification of Air Masses Responsible for Warm Events on the East Antarctic Coast

Naoyuki Kurita[1], Naohiko Hirasawa[2], Seizi Koga[3], Junji Matsushita[2], Hans Christian Steen-Larsen[4], Valérie Masson-Delmotte[5] and Yasushi Fujiyoshi[6]

[1]*Institute for Space-Earth Environmental Research*, *Nagoya University*, *Nagoya*, *Japan*
[2]*National Institute of Polar Research*, *Tachikawa*, *Tokyo*, *Japan*
[3]*National Institute of Advanced Industrial Science and Technology*, *Tsukuba*, *Ibaraki*, *Japan*
[4]*Centre for Ice and Climate*, *Niels Bohr Institute*, *University of Copenhagen*, *Kobenhavn*, *Denmark*
[5]*LSCE Laboratoire des Sciences du Climat et de l'nvironnement*, *Gif-sur-Yvette*, *Île-de-France*, *France*
[6]*Institute of Low Temperature Science*, *Hokkaido University*, *Sapporo*, *Japan*

Abstract

Warm events, periods when rising surface air temperatures can trigger surface melt, have been recorded during the austral summer at Syowa station on the East Antarctic coast. This study identifies air masses responsible for summer warm events at Syowa. Air masses arriving at Syowa are classified into marine and glacial sources based on their isotopic characteristics. Warm events are not associated with moist marine air intrusion, but with the downward flow of dry glacial air along the west side slope of the mountains in Enderby Land (EL). We use simulations from the Antarctic Mesoscale Prediction System (AMPS) to explore the atmospheric process responsible for the warmest event at Syowa. The model output illustrates several foehn-associated features such as low-level blocking, precipitation on the mountain's windward side, and mountain wave activity, with warm air ascending on the upstream slope and descending to Syowa. The foehn warming is caused by an easterly cross-mountain flow associated with a low-pressure system to the north of the EL coast. Future changes in synoptic cyclonic activity off the EL coast may have a significant impact on the frequency and intensity of foehn events at Syowa and the associated coastal warm events.

(**Citation**: Kurita, N., N. Hirasawa, S. Koga, J. Matsushita, H. C. Steen-Larsen, V. Masson-Delmotte, and Y. Fujiyoshi, 2016: Identification of air mass responsible for warm events on the East Antarctic coast. *SOLA*, **12**, 307−313, doi:10.2151/sola.2016-060.)

1. Introduction

In many coastal Antarctic regions, summer temperatures have reached positive values and triggered surface melt of glaciers and ice shelves (Trusel et al. 2015). For example, warming trends observed in the Antarctic Peninsula (AP) and West Antarctica (WA) in the past decades (Vaughan et al. 2003; Bromwich et al. 2012) have been associated with increase in mass loss (Mouginot et al. 2014; Sutterley et al. 2014). Present available observation dataset, however, is of insufficient length to address that these warming trends are anthropogenically forced, because natural interannual to multi-decadal variability may obscure these warming trends (Jones et al. 2016). While no significant warming trends have been recorded in East Antarctica (EA) in recent decades (Altnau et al. 2014), surface snowmelt is observed every summer over ice shelves, even in the East Antarctic coast (Toriensi et al. 2003; Picard and Fily 2006; Trusel et al. 2013). Even a slight increase in the summer air temperature on the East Antarctic coast therefore is expected to enhance surface melt and its role in ice loss. One research direction in order to understand mechanisms of coastal melt is to identify the key processes responsible for warm events, when surface air temperature rises beyond the melting point.

Greater transport of warm air from the ice-free ocean (marine air intrusion) is thought to be the main driver of recent regional warming trends in Antarctica. The summer warming of the AP over the last half of the 20th century, for example, is consistent with strengthened westerly marine air advection driven by changes in the Southern Hemisphere Annular Mode (SAM) (e.g., Marshall et al. 2006; Turner et al. 2016). This warm westerly flow travels over mountain ranges on the AP, causing additional temperature increase by adiabatic warming as the air descends on the east side of the AP that is called a foehn warming (e.g., Elvidge et al. 2015, 2016; Cape et al. 2015; Grosvenor et al. 2014). The increase in poleward marine air advection is also known to have contributed to summer warming at Byrd Station through most of the late 1980s, though it can not solely explain long-term trends in West Antarctica (Bromwich et al. 2012). Changes in the frequency, duration and magnitude of marine air intrusions therefore are expected to play a major role on the occurrence of melt on the coast of the East Antarctic ice sheet.

Here, we used atmospheric water vapor isotopologues (HDO and $H_2{}^{18}O$) to identify the origin of vapor and air masses moving to Syowa station. The isotopic composition is expressed by δ notation, a normalized difference of the isotopic ratio (R) from the isotopic ratio of Vienna Standard Mean Ocean Water (R_{vsmow}): $\delta = R/R_{vsmow} - 1$. As a second-order isotopic parameter, Dansgaard (1964) defined deuterium excess (d-excess) as $d = \delta D - 8\delta^{18}O$. The isotopic composition of coastal air masses in polar regions tends to reflect the relative contribution of marine versus glacial air masses (Kopec et al. 2014; Bonne et al. 2014). In earlier study of the marine air masses moving to Syowa, we identified the isotopic signatures of ocean evaporation through higher δD and lower d-excess than those of the summer average value (Kurita et al. 2016). In contrast, glacial air masses in the interior of the ice sheet are characterized by more depleted δD and higher d-excess values than those at Syowa (e.g., Casado et al. 2016; Ritter et al. 2016). The latter signal is explained by isotopic distillation and gradual loss of heavy isotopes associated with condensation and cooling when air masses travel over the Antarctic continent. During this process, an anti-phase is observed between δD and d-excess (Fujita and Abe 2006; Masson-Delmotte et al. 2008; Stenni et al. 2016). The pair of δD and d-excess measurements therefore permits to distinguish between marine air mass and glacial air mass at Syowa station.

In this study, we classify air masses arriving at Syowa into marine and glacial air masses based on these isotopic patterns. We then test whether marine air intrusions play a key role in warm events exceeding melting point at Syowa and explore atmospheric process responsible for warm events using air mass trajectory analysis and regional atmospheric model simulations.

Corresponding author: Naoyuki Kurita, Institute for Space-Earth Environmental Research, Nagoya University, Furo-cho, Chikusa-ku, Nagoya, Aichi, 464-8601, Japan. E-mail: kurita.naoyuki@e.mbox.nagoya-u.ac.jp.
©2016, the Meteorological Society of Japan.

2. Data and method

Water vapor isotopologues were continuously measured along the Japanese Antarctic Research Expedition (JARE) cruise track on the icebreaker *Shirase* during two austral summers (December–February (DJF)), 2013/2014 (JARE 55) and 2014/2015 (JARE 56) (Kurita et al. 2016). The H_2O concentration and water vapor isotopologues were monitored using laser spectroscopy every second and calibrated by a procedure that we described earlier (Kurita et al. 2012). Syowa station (69.00°'S, 39.58°'E) is located on East Ongul Island in Lutzow-Holm Bay in eastern Dronning Maud Land (DML), EA (Fig. 1). The *Shirase* moves around the Lutzow-Holm Bay near the Syowa area from late December to early February each year. In this study, we use hourly integrated isotope data recorded from the ship in Lutzow-Holm Bay. The analytical uncertainty is 2.5‰ for δD and 0.28‰ for δ^{18}O, which results in an uncertainty of 3.4‰ for d-excess.

Surface meteorological data are obtained from Syowa station. Hourly meteorological variables such as relative humidity, air temperature, wind speed, wind direction, incoming solar radiation, snowfall, and snow depth are available from the Japan Meteorological Agency (JMA; http://www.data.jma.go.jp/gmd/risk/obsdl). The Interim (ERA-I) (Dee et al. 2011) reanalysis dataset from the European Center for Medium-range Weather Forecasts (ECMWF) is used to examine synoptic-scale weather conditions. The ERA-I data are on a horizontal 0.75° × 0.75° grid with 37 vertical layers from 1000 to 1 hPa. The ERA-I has been found to effectively reproduce observed air temperature at a coastal station in Antarctica (Jones and Lister 2015; Simmonds et al. 2016).

The NOAA Hybrid Single-Particle Lagrangian Integrated Trajectory (HYSPLIT) Model (Version 4.0) (Draxler and Rolph 2003) is used with ERA-I for trajectory analysis to determine air mass transport pathways. HYSPLIT is run in ensemble mode, with 27 ensemble members initiated under different meteorological conditions (Draxler 2003). Each ensemble trajectory is computed from the fixed initial position (Syowa), while the meteorological data associated with each trajectory are offset by ±1 grid point (0.75° × 0.75°) in a horizontal direction and ±500 m in a vertical direction. A total of 27 (96-hour) isentropic backward trajectories were calculated at 0000 and 1200 UTC from Syowa while the *Shirase* remained in Lutzow-Holm Bay.

Weather forecast data from the Antarctic Mesoscale Prediction System (AMPS; Powers et al. 2003) are used to describe atmospheric features contributing to warm events at Syowa. AMPS employs the Polar Weather Research and Forecasting Model (Polar WRF), a version of the WRF optimized for high latitudes by the Polar Meteorology Group of the Byrd Polar Research Center at Ohio State University (Hines et al. 2008; Bromwich et al. 2009; Hines et al. 2011). Initial and boundary conditions for AMPS forecasts are taken from the National Centers for Environmental Prediction Global Forecast System. The model uses three-dimensional variational data assimilation (Barker et al. 2004). Each AMPS forecast is configured to have six domains, with a horizontal resolution ranging from 30 km for the outer domain over about half of the Southern Hemisphere, to 1 km over McMurdo in the western Ross Sea. In this study we used AMPS forecasts of the 10 km Antarctic grid (domain 2) with sixty vertical levels. The forecasts are run twice daily, with initialization at 0000 and 1200 UTC. Forecast length is 120-h for the 30 km resolution. We minimize the effect of initial conditions by discarding the first 6 h forecasts for the model spin-up. The AMPS output has been successfully used to model mesoscale atmospheric dynamics over the Antarctica (e.g., Schlosser et al. 2008; Schlosser et al. 2010; Speirs et al. 2010; Nicolas and Bromwich 2011; Cape et al. 2015).

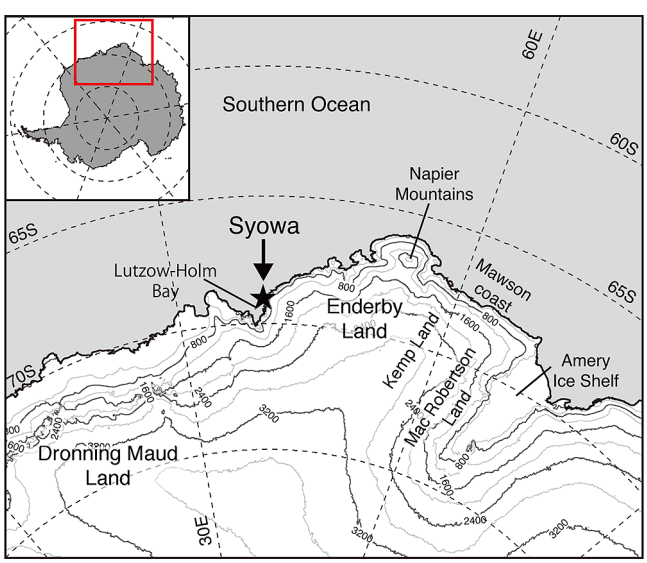

Fig. 1. Topographic map of East Antarctica around the location of the Syowa station with elevation contours plotted at 400 m intervals. The shaded black star shows Syowa station.

3. Warm temperature events in summer at Syowa

3.1 Do marine air intrusions play a key role in warm events at Syowa?

Figure 2 plots the time series of the normalized δD and d-excess anomalies in surface vapor while the *Shirase* remained in Lutzow-Holm Bay, together with precipitation, temperature, and relative humidity variations at Syowa. Hourly anomalies were calculated with respect to the average of two austral summers (2013/2014 and 2014/2015) and then normalized by standard deviation. δD and d-excess variations in surface vapor show weak diurnal variability with dominant day-to-day fluctuations. The relative lack of diurnal change in δD and d-excess suggests that the isotopic variability reflects regional-scale circulation rather than local processes such as boundary layer dynamics or the local evaporation sources observed in the inland stations (e.g., Casado et al. 2016; Ritter et al. 2016). Because the humidity data measured hourly on the *Shirase* correlates well with the humidity data from Syowa during the observation period (R = 0.90), we can assume that the isotopic variability on the ship represents that at Syowa. Figure 2 also shows the time series of temperature at 2 m and relative humidity from the AMPS forecast at the closest grid. AMPS underestimates the day-to-day minimum surface air temperature (T_{min}) and accordingly shows a cold bias for the daily average temperature (T_a). AMPS does, however, moderately reproduce the observed day-to-day variations. Note that strong dry conditions are observed and simulated by AMPS when the daily maximum surface air temperature (T_{max}) rises above the melting point (e.g., 29−30 December 2013 and 22−23 December 2014). ERA-I fails to reproduce these dry conditions, although it does perform fairly well in producing the diurnal cycle and day-to-day variation in the surface air temperature observed during the two austral summers (not shown).

In this study we define a warm event as a period when T_a rises above the melting point (> 0.5°C), and T_{max} exceeds 2°C. During the summer of JARE 55, two successive warm events were recorded: one from 29 December 2013 to 4 January 2014 and the other from 13 to 17 January 2014 (purple shading in Fig. 2a). Moreover, during the summer of JARE 56, we observed a rise of T_{max} to 7.8°C during a remarkably warm event in late December (20−26 December 2014) as displayed in Fig. 2b. We will begin here by exploring the role of marine air advection from the ice-free ocean in these warm events. According to our earlier investigation, marine air advecting from the ice-free ocean to Syowa is characterized by a higher δD and lower d-excess, compared to the average values in summer (DJF) (Kurita et al. 2016). Based on this finding, periods when marine air masses dominate over Syowa are identified as positive δD and negative d-excess anomalies (yellow shading in Fig. 2). We used trajectory analysis to confirm the identification of marine air masses based on the isotopic char-

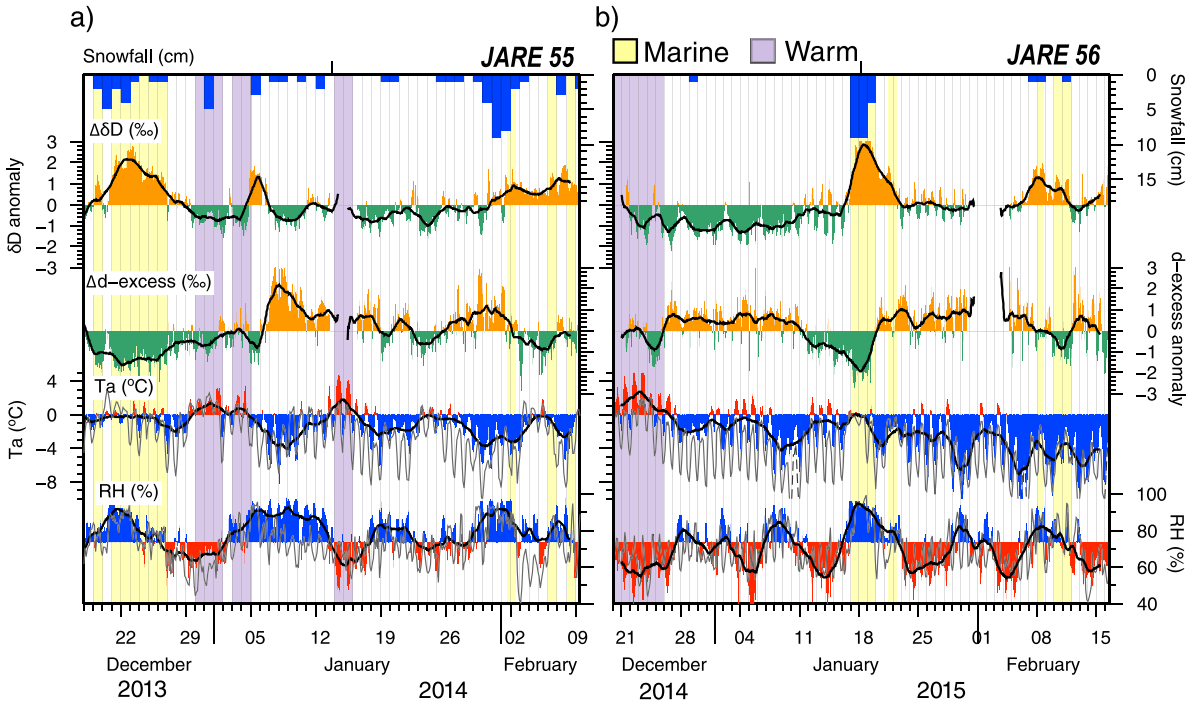

Fig. 2. (a) Time series of δD and d-excess anomalies in surface vapor observed at the icebreaker *Shirase*, and air temperature, relative humidity, and snowfall (blue bar at the top of the panel) at Syowa station while the *Shirase* moved around the Lutzow-Holm Bay during the JARE 55 cruise (16 December 2013~09 February 2014). Anomalies with respect to the austral summer average in the observation years (2013/2014 and 2014/2015) are normalized by standard deviation and represented by orange (green) bars. Temperatures above (below) the melting point are represented by red (blue) bars. Relative humidity below (above) the austral summer average (74%) is represented by red (blue) bars. The solid black curves represent the two day moving average. The dark gray lines indicate the AMPS 2 m air temperature and relative humidity at the grid point nearest to Syowa. Background colors indicate the period when marine air masses dominated over Syowa (yellow) and warm periods associated with a T_a above the melting point and T_{max} exceeding 2°C (purple). Light gray line represents the boundary of a day (UTC). (b) The same time series shown in Fig. 2a, but for the JARE 56 cruise (20 December 2014~16 February 2015).

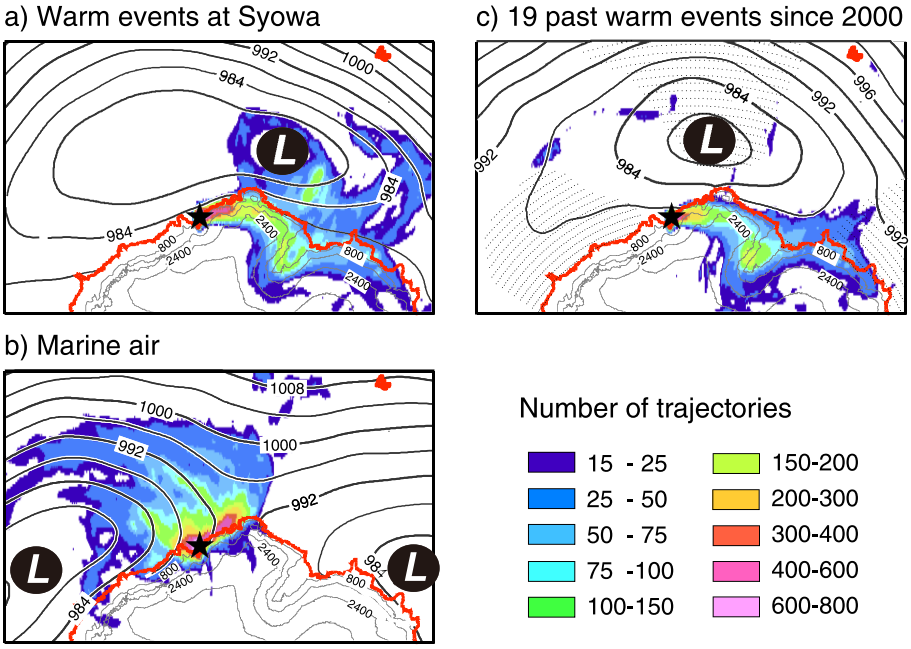

Fig. 3. A composite back trajectory patterns for the Syowa (black circle) during: (a) warm periods (purple shading in Fig. 2), (b) periods when marine air masses dominated (yellow shading in Fig. 2). The background color field represents trajectory counts at 30 minute intervals on a 0.75° × 0.75° grid. Total number of trajectories is 756 for both periods. A composite map of sea surface pressure (SLP, solid lines, contour interval 4 hPa) during each of the periods is shown. Sea level pressure data above 150 m elevation is masked. Topographic contours are plotted at 800 m interval over the Antarctic continent. (c) The same composite back trajectory patterns shown in Fig. 3a, but for past warm events observed from Syowa between the summers of 2000 and 2013 (19 cases). Total number of trajectories for these events is 513. Dotted areas denote that the composite SLP field is statistically significant at a 99% confidence level.

acteristics. Figure 3 shows a composite map of back trajectories for Syowa during periods when positive δD and negative d-excess anomalies were observed. The major trajectory paths reveal that air masses are transported by cyclonic flow along the eastern flank of a coastal cyclone over the Southern Ocean. This result supports our classification based on the isotopic characteristics. The large positive δD peaks paired with lowermost negative d-excess anomalies in Figs. 2a and 2b correspond to sustained marine air intrusions over two periods of several days (21−26 December 2013 and 17−19 January 2015). These two periods were associated with passages of strong precipitation events, so-called atmospheric river (AR): poleward moisture was organized in a filamentary structure stretching from subtropical latitudes to Antarctica, leading to heavy snow accumulation events over DML (Gorodetskaya et al. 2014). Note that, in Greenland, an AR event was observed in summer 2012 (e.g., Neff et al. 2014), including water vapor isotope monitoring (Bonne et al. 2015), and let to widespread melt at the ice sheet surface (Nghiem et al. 2012). As observed over the Greenland ice sheet, T_{max} rose at Syowa above the melting point during these events. This warming, however, was much smaller than the temperature measured during another warm events (see purple shading in Figs. 2a and 2b). The fact that the warmest periods were characterized by negative δD anomalies as well as dry conditions suggests, paradoxically, that warm events are caused by advection of glacial air masses rather than marine air intrusion. The major trajectory paths for warm events show air mass trajectories travelling over the ice sheet from the Mac Robertson Land (MRL) across the Enderby Land (EL) (Fig. 3a).

3.2 Atmospheric process responsible for warm events

The most remarkable warm period in our observations started on 20 December 2014 and lasted 7 days. The highest temperature reached, 7.8°C, was recorded in the afternoon (1200 UTC) of 23 December 2014. The air temperatures on that day stayed above 0.8°C even in the midnight hours, and the relative humidity dropped below 40%. Figures 4 and 5 show the horizontal and vertical atmospheric conditions of this warm event from the AMPS forecast. As mentioned above, AMPS successfully simulates the strong dry condition during this event, although the model underestimates T_{max} (+1.9°C). In Fig. 4a, the synoptic-scale atmospheric condition is characterized by a meridional pressure gradient enhanced by a low pressure centered in the north of the EL coast. Strong easterly winds flowing over the mountains of EL prevail during the warmest event. The longitude-height plot of the backward trajectory for this event shows that the air masses ascending the slope in the MRL and passing over the mountain ranges go on to descend the west side of the EL mountain slope to Syowa (purple line drawn in Fig. 5a). Furthermore, Fig. 4b illustrates that the temperature over the lee-side of the EL coast is considerably higher than that on the windward side. These results suggest that the warmest event might result from foehn warming: the drawdown of potentially warmer air from aloft (isentropic drawdown); precipitation resulting in latent heat release over the mountains (latent heating and precipitation); mechanical mixing of the stably stratified airmass over the mountains (mechanical mixing); and radiative warming (radiative heating) as a result of the dry, commonly cloud-free foehn conditions (see Elvidge and Renfrew (2016) for a comprehensive explanation of the foehn warming mechanism).

The foehn phenomena is characterized by a downslope flow acceleration that occurs as a result of the interaction between the mountain topography and atmospheric flow impinging the mountains. The downslope wind response to cross-mountain flow depends on whether the upstream flow approaches the mountains under linear or non-linear conditions (see Durran (1990) for a detailed review). To quantify flow linearity (nonlinearity), we calculate the non-dimensional mountain height, also known as the inverse Froude number, $\hat{h} = Nh/U$, where N is the upstream Brunt-Väisälä frequency, h is the mountain height, and U is the upstream vertically averaged wind speed (between 500 and 3000 m). Variables U and N are obtained at 190 km east of the mountains, where the upwind flow is unaffected by the mountain (location at the eastern edge of the Fig. 5d). For the warmest event, $\hat{h}$ of 2.4 is found at 1200 UTC 22 December 2014, indicating significant nonlinearity ($\hat{h} > 1$). With this information, we can characterize the upwind flow as a strongly stratified, slowly moving flow leading to blockage of low-level flow, mountain wave breaking, and downslope wind acceleration accompanied by mountain wave systems (Durran 1990). The isentropes shown in a cross-section of the potential temperature along the air mass trajectory are identical with the streamlines in the flow. Figure 5 illustrates these foehn-associated features. In Fig. 5d, for example,

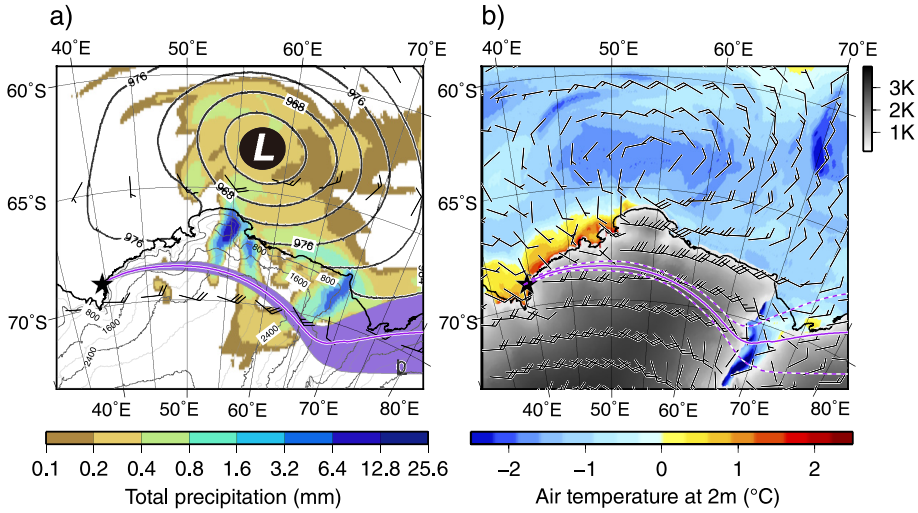

Fig. 4. (a) A composite map of the AMPS forecast over the period when the air mass responsible for the warm event on 23 December 2014 moves across the mountainous region in East Antarctica (1200 UTC 22 December−1200 UTC 23 December). The map depicts the 24 hour average of SLP (black contours, contour interval 4 hPa), near-surface wind vectors (black arrows), and precipitation (shading). The 24 hour average is calculated from 12, 15, 18, 21, and 24 hour forecasts initialized at 0000 UTC on 22 December 2014 and 6, 9, and 12 hour forecasts initialized at 1200 UTC 23 December 2014. Note that the SLP is masked over regions exceeding 150 m elevation. Gray contours over Antarctica represent the topography at 400 m intervals. The purple line shows the mean position of 27 air mass trajectories launched from Syowa (black star) at 1200 UTC on 23 December 2014. The purple shaded envelope represents the standard deviation (1σ) of the 27 trajectories. (b) AMPS forecast for 1200 UTC 23 December 2014 (12 hour forecast initialized at 0000 UTC), showing near-surface wind vectors (black arrows), and the surface temperature at 2 m (shading). Note that the surface temperature is masked over regions exceeding 300 m elevation. Topography is shaded in gray. The purple solid and dashed lines represent the trajectory shown in Fig. 4a.

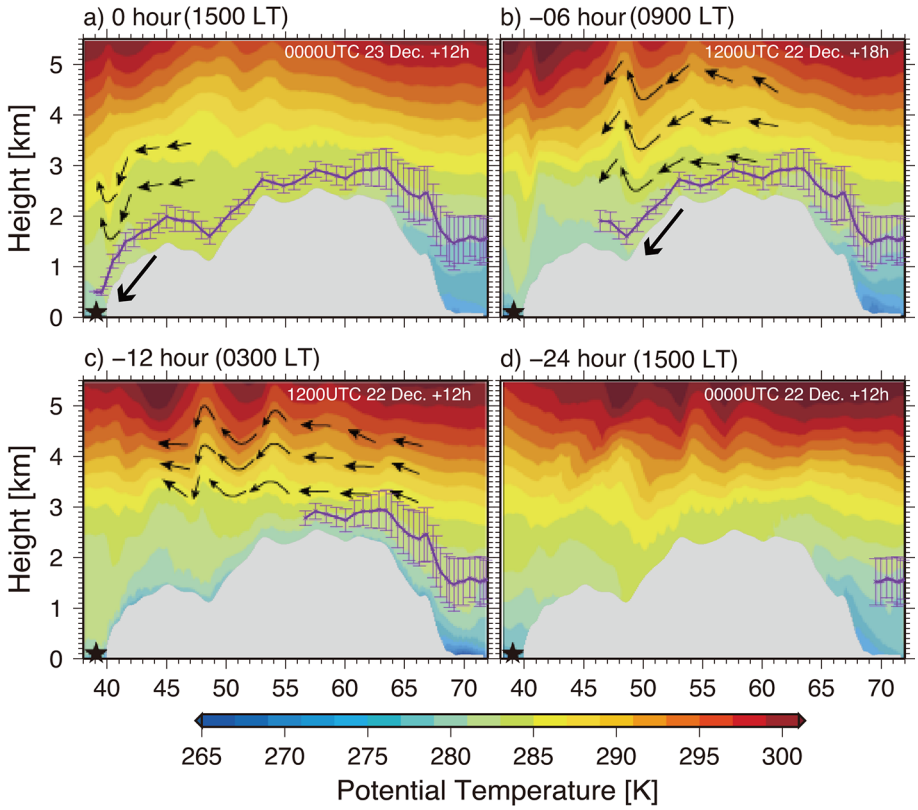

Fig. 5. Vertical cross section of the potential temperature (shading, K) along the air mass trajectory shown in Fig. 4 (a) when the air mass arrives at Syowa at 1200 UTC on 23 December 2014 and (b), (c), (d) at 6 hours, 12 hours, and 24 hours before the air mass arrives at Syowa, respectively, according to the AMPS forecast. The model initialization time and forecast hour are shown in the upper right-hand corner (white characters). The gray shading shows the topography. The purple line represents the position of the air mass and trajectory shown in Fig. 4. The error bars represent the standard deviations of the 27 trajectories. The black star represents Syowa station. Black arrows show foehn-associated flow.

low-level blocking is apparent upwind of the mountain. Above the mountain, mountain waves are present when air masses flow over the chain of mountain ridges (Fig. 5c). The downward displacement of isentropes and its overturning above the lee slope that is called a hydraulic jump reflect the mountain wave breaking (e.g., Durran 1986) (Figs. 5a and 5b). The descending isentropes along the lee slope cause the accelerated downslope winds (Fig. 5a). An important feature of a nonlinear foehn event is that the air masses causing foehn warming originate near or above the mountain top level. As shown in Fig. 5d, a strong inversion is apparent at 1000~1300 m when air masses approach the upwind side of the mountain. The upwind trajectory altitude corresponds to just above this inversion (1500 m). The isentropic drawdown of this warm air could therefore explain a large part of the foehn warming observed. In Antarctica, this type of foehn warming (nonlinear foehn event) has been observed on the east side of the AP (Elvidge et al. 2015, 2016; Cape et al. 2015; Grosvenor et al. 2014) and in the McMurdo dry valleys of EA (Speirs et al. 2010; Steinhoff et al. 2013, 2014). We cannot, however, ignore the contribution of the latent heating of precipitation. Figure 4a shows precipitation occurring on the windward side of the mountain. The latent heating of the precipitation also may warm the descending air at the low-lying ice shelves near Syowa before it ascends on the windward side. Two other foehn mechanisms: mechanical mixing and radiative heating, seem to be of some importance for the warmest event in December 2014, as changes of the equivalent potential temperatures in air masses are less than 1 K over the mountains (not shown).

Finally, we examine the isotopic signature for the warm event based on the dynamics of the nonlinear foehn event. As a rule of thumb, the δD of water vapor gradually decreases with altitude, which reflects the integrated history of condensation (e.g., Ehhalt et al. 2005). While none of the previous observational studies have described the vertical profile of d-excess, calculated d-excess from isotopic profiles reported by He and Smith (1999) showed that the d-excess values at the top of a boundary layer are significantly higher than those at the surface. From these results, we can speculate that the δD (d-excess) values of water vapor impinging on the mountain region are lower (higher) than those for the marine air mass. We also know that the additional loss of heavy isotopes as precipitation results in further decreases of the δD of water vapor. D-excess is relatively invariant during a condensation process, except under a lower temperature condition. We can thus reasonably assume that the air masses for the warm event contain fewer heavy isotopes and higher d-excess values than marine air. It is consistent with the observed isotopic characteristics for the warm events. While research to gain a quantitative understanding of the observed warm events continues, this study gives us preliminary evidence that the two mechanisms of isentropic drawdown and latent heating and precipitation contribute the warm events at Syowa. We could gain a better understanding of the role of foehn warming in the Syowa climate by installing a monitoring network from the windward regions to Syowa.

4. Discussion and conclusions

Isotopic features enabled us to classify air masses arriving at Syowa station into oceanic (marine air) and glacial (glacial air) origins. Warm weather events observed at Syowa over two observed austral summers were associated not with marine air, but with glacial air descending from the interior of the ice sheet to Syowa. This glacial air was transported by easterlies passing over mountain ranges in EA, producing a nonlinear foehn event with a key role in these warm events. This result, however, is based solely on a single warm event observed on 23 December 2014.

Further investigation will be necessary to determine whether the foehn warming is the single key factor in generating these warm events.

We therefore examined past warm events from 2000 to 2014 to determine whether the foehn effect played a key role. Figure 3c illustrates air mass trajectories for 19 events in which T_a rose above the melting point, and T_{max} exceeded 2°C at Syowa. Past warm events are also associated with a low pressure centered in the north of the EL coast driving a strong easterly air flow impinging on the MRL mountain range. Most warm events were also found to have occurred on dry sunny days, which was consistent with the warm events observed in the 2013/2014 and 2014/2015 summers. We therefore conclude that this type of synoptic weather plays a key role in warm events at Syowa. If these warm events recur more often in the future, melt events can also be expected to become more frequent in coastal Eastern Antarctica. Early signs of climate change in EA could therefore be detected by closely monitoring of these events at coastal sites. Given the ERA-I's lack of resolution to sufficiently capture the foehn events, a high-resolution numerical model to appropriately resolve the complex topography over the Antarctic coast, such as AMPS, will be critical to gain a quantitative understanding of the influence of foehn warming on the East Antarctica climate and improve our projections of the coastal Antarctic surface melt and mass balance. The isotopic composition of water vapor above the Antarctic ice sheet will be an important diagnostic tool to assess the performance of the model used. Lastly, a better quantitative understanding of the isotopic composition in water vapor would enable us to more precisely depict the hydrological cycle over the Antarctic ice sheet.

Acknowledgments

This study was supported by JSPS KAKENHI grant 25550022 and grant for Joint Research Program of the Institute of Low Temperature Science, Hokkaido University. The authors gratefully acknowledge the NOAA Air Resources Laboratory (ARL) for the provision of the HYSPLIT transport and dispersion model and the relevant input files for generation of backward trajectories. The ERI-data are available via the ECMWF data portal (http://apps.ecmwf.int/datasets/data/interim-full-daily). AMPS forecast products are available from the National Center for Atmosphere (https://www.earthsystemgrid.org/dataset/ucar.mmm.amps.wrf_30.201412.html). We also thank two anonymous reviewers for constructive comments on the manuscript.

Edited by: T. Kawano

References

Altnau, S., E. Schlosser, E. Isaksson, and D. Divine, 2014: Climatic signals from 76 shallow firn cores in Dronning Maud Land, East Antarctica. *The Cryosphere*, **9**, 925−944.

Barker, D. M., W. Huang, Y. R. Guo, A. J. Bourgeois, and Q. N. Xiao, 2004: A Three-dimensional variational data assimilation system for MM5: Implementation and initial results. *Mon. Wea. Rev.*, **132**, 897−914.

Bonne, J. L., V. Masson-Delmotte, O. Cattani, M. Delmotte, C. Risi, H. Sodemann, and H. C. Steen-Larsen, 2014: The isotopic composition of water vapour and precipitation in Ivittuut, southern Greenland. *Atmos. Chem. Phys.*, **14**, 4419−4439.

Bonne, J.-L., H. C. Steen Larsen, C. Risi, M. Werner, H. Sodemann, J.-L. Lacour, X. Fettweis, G. Cesana, M. Delmotte, O. Cattani, P. Vallelonga, H. A. Kjaer, C. Clerbaux, Á. E. Sveinbjörnsdóttirffilmark, and V. Masson-Delmotte, 2015: The summer 2012 Greenland heat wave: in situ and remote sensing observations of water vapour isotopic composition during an atmospheric river event. *J. Geophys. Res.*, **120**, 2970−2989.

Bromwich, D. H., K. M. Hines, and L. S. Bai, 2009: Development and testing of polar weather research and forecasting model: 2. Arctic ocean. *J. Geophys. Res.*, **114**, doi:10.1029/2008JD010300.

Bromwich, D. H., J. P. Nicolas, A. J. Monaghan, M. A. Laz zara, L. M. Keller, G. A. Weidner, and A. B. Wilson, 2012: Central West Antarctica among the most rapidly warming regions on Earth. *Nat. Geosci.*, **6**, 1−7.

Casado, M., A. Landais, V. Masson-Delmotte, C. Genthon, E. Kerstel, S. Kassi, L. Arnaud, G. Picard, F. Prie, O. Cattani, H. C. Steen-Larsen, E. Vignon, and P. Cermak, 2016: Continuous measurements of isotopic composition of water vapour on the East Antarctic Plateau. *Atmos. Chem. Phys.*, **16**, 8521−8538.

Cape, M. R., M. Vernet, P. Skvarca, S. Marinesk, T. Scambos, and E. Domack, 2015: Foehn winds link climate-driven warming to ice shelf evolution in Antarctica. *J. Geophys. Res.*, **120**, 11037−11057.

Dansgaard, W., 1964: Stable isotopes in precipitation. *Tellus*, **16**, 436−468.

Dee, D. P., S. M. Uppala, A. J. Simmons, P. Berrisford, P. Poli, S. Kobayashi, U. Andrae, M. A. Balmaseda, G. Balsamo, P. Bauer, P. Bechtold, A. C. M. Beljaars, L. van de Berg, J. Bidlot, N. Bormann, C. Delsol, R. Dragani, M. Fuentes, A. J. Geer, L. Haimberger, S. B. Healy, H. Hersbach, E. V. Hólm, L. Isaksen, P. Kållberg, M. Köhler, M. Matricardi, A. P. McNally, B. M. Monge-Sanz, J. J. Morc rette, B. K. Park, C. Peubey, P. de Rosnay, C. Tavolato, J. N. Thépaut, and F. Vitart, 2011: The ERA-Interim reanalysis: Configuration and performance of the data assimilation system. *Quart. J. Roy. Meteor. Soc.*, **137**, 553−597.

Draxler, R., and G. Rolph, 2003: Hybrid Singlee-Particle Lagrangian Integrated Trajectory (HYSPLIT), model released from NOAA ARL READY NOAA Air Resources Laboratory, Silver Spring, MD. (Available online at http://ready.arl.noaa.gov/HYSPLIT.php, accessed 30 April 2014).

Draxler, R. R., 2003: Evaluation of an ensemble dispersion calculation. *J. Appl. Geophys.*, **42**, 308−317.

Durran, D. R., 1986: Part I: The development of analogs to supercritical flow in an infinitely deep, continuously stratified fluid. *J. Atmos. Sci.*, **43**, 2527−2543.

Durran, D. R., 1990: Mountain waves and downslope winds. *Atmospheric Processes over Complex Terrain*, W. Blumen, Ed., Amer. Meteor. Soc., 59−81.

Ehhalt, D. H., F. Rohrer, and A. Fried, 2005: Vertical profiles of HDO/H2O in the troposphere. *J. Geophys. Res.*, **110**, doi:10.1029/2004JD005569.

Elvidge, A. D., I. A. Renfrew, J. C. King, A. Orr, T. A. Lachlan-Cope, M. Weeks, and S. L. Gray, 2015: Foehn jets over the Larsen C Ice shelf, Antarctica. *Quart. J. Roy. Meteor. Soc.*, **141**, 698−713.

Elvidge, A. D., and I. A. Renfrew, 2016: The causes of foehn warming in the lee of mountains. *Bull. Amer. Meteor. Soc.*, **97**, 455−466.

Elvidge, A. D., I. A. Renfrew, J. C. King, A. Orr, and T. A. Lachlan-Cope, 2016: Foehn warming distributions in nonlinear and linear flow regimes: a focus on the Antarctic Peninsula. *Quart. J. Roy. Meteor. Soc.*, **142**, 618−631.

Fujita, K., and O. Abe, 2006: Stable isotopes in daily precipitation at Dome Fuji, East Antarctica. *Geophys. Res. Lett.*, **33**, doi:10.1029/2006GL026936.

Gorodetskaya, I. V., M. Tsukernik, K. Claes, M. F. Ralph, W. D. Neff, and N. P. M. Van Lipzig, 2014: The role of atmospheric rivers in anomalous snow accumulation in East Antarctica. *Geophys. Res. Lett.*, **41**, 6199−6206.

Grosvenor, D. P., J. C. King, T. W. Choularton, and T. Lachlan-Cope, 2014: Downslope föhn winds over the Antarctic Peninsula and their effect on the Larsen ice shelves. *Atmos. Chem. Phys.*, **14**, 9481−9509.

He, H., and R. B. Smith, 1999: Stable isotope composition of water vapor in the atmospheric boundary layer above the forests of New England. *J. Geophys. Res.*, **104**, 11657−11673.

Hines, K. M., and D. H. Bromwich, 2008: Development and testing of Polar Weather Research and Forecasting (WRF)

Model. Part I: Greenland ice sheet meteorology. *Mon. Wea. Rev.*, **136**, 1971−1989.

Hines, K. M., D. H. Bromwich, L.-S. Bai, M. Barlage, and A. G. Slater, 2011: Development and testing of Polar WRF. part III: Arctic land. *J. Climate*, **24**, 26−48.

Jones, P. D., and D. H. Lister, 2015: Antarctic near-surface air temperatures compared with ERA-Interim values since 1979. *Int. J. Climatol.*, **35**, 1354−1366.

Jones, J. M., S. T. Gille, H. Goosse, N. J. Abram, P. O. Canziani, D. J. Charman, K. R. Clem, X. Crosta, C. de Lavergne, I. Eisenman, M. H. England, R. L. Fogt, L. M. Frankcombe, G. J. Marshall, V. Masson-Delmotte, A. K. Morrison, A. J. Orsi, M. N. Raphael, J. A. Renwick, D. P. Schneider, G. R. Simpkins, E. J. Steig, B. Stenni, D. Swingedouw, and T. R. Vance, 2016: Assessing recent trends in high-latitude Southern Hemisphere surface climate. *Nat. Clim. Chang.*, **6**, 917−926.

Kopec, B. G., A. M. Lauder, E. S. Posmentier, and X. Feng, 2014: The diel cycle of water vapor in West Greenland. *J. Geophys. Res.*, **119**, 9386−9399.

Kurita, N., B. D. Newman, L. J. Araguás-Araguás, and P. Aggarwal, 2012: Evaluation of continuous water vapor δd and δ^{18}O measurements by off-axis integrated cavity output spectroscopy. *Atmos. Meas. Tech.*, **5**, 2069−2080.

Kurita, N., N. Hirasawa, S. Koga, J. Matsushita, H. C. Steen-Larsen, V. Masson-Delmotte, and Y. Fujiyoshi, 2016: Influence of large-scale atmospheric circulation on marine air intrusion toward the East Antarctic coast. *Geophys. Res. Lett.*, **43**, 9298−9305.

Marshall, G. J., A. Orr, N. P. M. Van Lipzig, and J. C. King, 2006: The impact of a changing southern hemisphere annular mode on Antarctic Peninsula Summer Temperatures. *J. Climate*, **19**, 5388−5404.

Masson-Delmotte, V., S. Hou, A. Ekaykin, J. Jouzel, A. Aristarain, R. T. Bernardo, D. Bromwich, O. Cattani, M. Delmotte, S. Falourd, M. Frezzotti, H. Gallée, L. Genoni, E. Isaksson, A. Landais, M. M Helsen, G. Hoffmann, J. Lopez, V. Morgan, H. Motoyama, D. Noone, H. Oerter, J. R. Petit, A. Royer, R. Uemura, G. A. Schmidt, E. Schlosser, J. C. Simões, E. J. Steig, B. Stenni, M. Stievenard, M. R. van den Broeke, R. S. W. van de Wal, W. J. van de Berg, F. Vimeux, and J. W. C. White, 2008: A review of Antarctic surface snow isotopic composition: observations, atmospheric circulation, and Isotopic modeling. *J. Climate*, **21**, 3359−3387.

Mouginot, J., E. Rignot, and B. Scheuchl, 2014: Sustained increase in ice discharge from the Amundsen sea embayment, West Antarctica, from 1973 to 2013. *Geophys. Res. Lett.*, **41**, 1576−1584.

Neff, W., G. P. Compo, F. Martin Ralph, and M. D. Shupe, 2014: Continental heat anomalies and the extreme melting of the Greenland ice surface in 2012 and 1889. *J. Geophys. Res. Atmos.*, **119**, 6520−6536.

Nghiem, S. V., D. K. Hall, T. L. Mote, M. Tedesco, M. R. Albert, K. Keegan, C. A. Shuman, N. E. DiGirolamo, and G. Neumann, 2012: The extreme melt across the Greenland ice sheet in 2012. *Geophys. Res. Lett.*, **39**, doi:10.1029/2012GL053611.

Nicolas, J. P., and D. H. Bromwich, 2011: Climate of West Antarctica and influence of marine air intrusions. *J. Climate*, **24**, 49−67.

Picard, G., and M. Fily, 2006: Surface melting observations in Antarctica by microwave radiometers: Correcting 26-year time series from changes in acquisition hours. *Remote Sens. Environ.*, **104**, 325−336.

Powers, J. G., A. J. Monaghan, A. M. Cayette, D. H. Bromwich, Y.-H. Kuo, and K. W. Manning, 2003: Real-time mesoscale modeling over Antarctica: the Antarctic Mesoscale Prediction System. *Bull. Amer. Meteor. Soc.*, **84**, 1533−1545.

Ritter, F., H. C. Steen Larsen, M. Werner, V. Masson-Delmotte, A. Orsi, M. Behrens, G. Birnbaum, J. Freitag, C. Risi, and S. Kipfstuhl, 2016: Isotopic exchange on the diurnal scale between near-surface snow and lower atmospheric water vapor at Kohnen station, East Antarctica. *The Cryosphere*, **10**, 1647−1663.

Schlosser, E., M. G. Duda, J. G. Powers, and K. W. Manning, 2008: Precipitation regime of Dronning Maud Land, Antarctica, derived from Antarctic Mesoscale Prediction System (AMPS) archive data. *J. Geophys. Res.*, **113**, doi:10.1029/2008JD009968.

Schlosser, E., J. G. Powers, M. G. Duda, K. W. Manning, C. H. Reijmer, and M. R. van den Broeke, 2010: An extreme precipitation event in Dronning Maud Land, Antarctica: A case study with the Antarctic Mesoscale Prediction System. *Polar Res.*, **29**, 330−344.

Simmons, A., P. Berrisford, D. Dee, H. Hersbach, S. Hirahara, and J. Thepaut, 2016: Estimates of variations and trends of global surface temperature. *ERA Report Series.*, **25**, 1−33.

Speirs, J. C., D. F. Steinhoff, H. A. McGowan, D. H. Bromwich, and A. J. Monaghan, 2010: Foehn winds in the McMurdo dry valleys, Antarctica: the origin of extreme warming events. *J. Climate*, **23**, 3577−3598.

Steinhoff, D. F., D. H. Bromwich, and A. Monaghan, 2013: Dynamics of the foehn mechanism in the McMurdo dry valleys of Antarctica from Polar WRF. *Quart. J. Roy. Meteor. Soc.*, **139**, 1615−1631.

Steinhoff, D. F., D. H. Bromwich, J. C. Speirs, H. A. McGowan, and A. J. Monaghan, 2014: Austral summer foehn winds over the McMurdo dry valleys of Antarctica from Polar WRF. *Quart. J. Roy. Meteor. Soc.*, **140**, 1825−1837.

Stenni, B., C. Scarchilli, V. Masson-Delmotte, E. Schlosser, V. Ciardini, G. Dreossi, P. Grigioni, M. Bonazza, A. Cagnati, D. Karlicek, C. Risi, R. Udisti, and M. Valt, 2016: Three-year monitoring of stable isotopes of precipitation at Concordia Station, East Antarctica. *The Cryosphere*, **10**, 2415−2428.

Sutterley, T. C., I. Velicogna, E. Rignot, J. Mouginot, T. Flament, M. R. van den Broeke, J. M. van Wessem, and C. H. Reijmer, 2014: Mass loss of the Amundsen sea embayment of West Antarctica from four independent techniques. *Geophys. Res. Lett.*, **41**, 8421−8428.

Torinesi, O., M. Fily, and C. Genthon, 2003: Variability and trends of the summer melt period of Antarctic Ice margins since 1980 from microwave sensors. *J. Climate*, **16**, 1047−1060.

Trusel, L. D., K. E. Frey, S. B. Das, P. K. Munneke, and M. R. van den Broeke, 2013: Satellite-based estimates of Antarctic surface meltwater fluxes. *Geophys. Res. Lett.*, **40**, 6148−6153.

Trusel, L. D., K. E. Frey, S. B. Das, B. Karnauskas, P. K. Munneke, E. van Meijgaard, and M. R. van den Broeke, 2015: Divergent trajectories of Antarctic surface melt under two twenty-first-century climate scenarios. *Nat. Geosci.*, **8**, 927−932.

Turner, J., H. Lu, I. White, J. C. King, T. Phillips, J. S. Hosking, T. J. Bracegirdle, G. J. Marshall, R. Mulvaney, and P. Deb, 2016: Absence of 21st century warming on Antarctic Peninsula consistent with natural variability. *Nature*, **535**, 411−415.

Vaughan, D. G., G. J. Marshall, W. M. Connolley, C. Parkinson, R. Mulvaney, D. A. Hodgson, J. C. King, C. J. Pudsey, and J. Turner, 2003: Recent rapid regional climate warming on the Antarctic Peninsula. *Climatic Change*, **60**, 243−274.

Manuscript received 25 July 2016, *accepted 21 October 2016*
SOLA: *https://www.jstage.jst.go.jp/browse/sola/*